Myelin surfactant assemblies shaping the electrodeposition of copper dendrites.

*José Ferreira[1], Jeroen Michiels[2], Marty Herregraven[2] & Peter A. Korevaar[1,]**

1) Institute for Molecules and Materials, Radboud University, Heyendaalseweg 135, Nijmegen 6525 AJ, The Netherlands
2) TechnoCentre, Faculty of Science, Radboud University, Heyendaalseweg 135, Nijmegen 6525 AJ, The Netherlands
Email: p.korevaar@science.ru.nl

ABSTRACT: Self-organization of inorganic matter enables bottom-up construction of materials with targetted shapes suited to their function. Positioning the building blocks in the growth process involves a well-balanced interplay of reaction and diffusion. Whereas (supra)molecular structures have been used to template such growth processes, we reasoned that molecular assemblies can be employed to actively create concentration gradients which shape the deposition of solid, wire-like structures. The core of our approach comprises the interaction between myelin assemblies that deliver copper(II) ions to the tips of copper dendrites, which in turn grow along the Cu^{2+}-gradient upon electrodeposition. First, we successfully include Cu^{2+} ions amongst amphiphile bilayers in myelin filaments, which grow from $C_{12}E_3$-based source droplets over air-water interfaces. Second, we characterize the growth of dendritic copper structures upon electrodeposition from a negative electrode at the sub-mM Cu^{2+} concentrations that are anticipated upon release from the copper loaded myelins. Third, we assess the intricate growth of copper dendrites upon electrodeposition, when combined with copper loaded myelins. The myelins deliver Cu^{2+} at a negative electrode, feeding copper dendrite growth upon electrodeposition. Intriguingly, the copper dendrites follow the Cu^{2+} gradient towards the myelins, and grow along them towards the source droplet. We demonstrate the growth of dynamic connections amongst electrodes and surfactant droplets in reconfigurabe setups – featuring a unique interplay between molecular assemblies and inorganic, solid structures. With the growing interest in neuromorphic circuitry, we envision such a self-organizing system opening entirely new pathways for interconnected networks of (semi)conductive wires that are integrated with soft-matter based systems.

key words: *self-assembly, self-organization, responsive materials, soft matter, gradients*

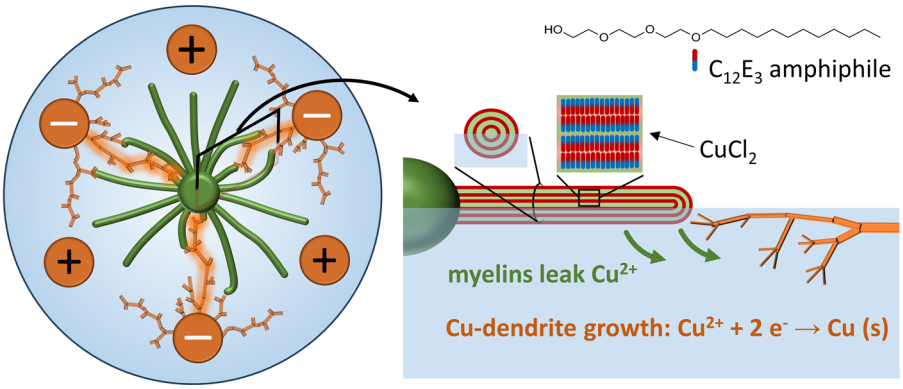

https://doi.org/10.26434/chemrxiv-2024-qhmqn **ORCID:** https://orcid.org/0000-0002-3395-7197 Content not peer-reviewed by ChemRxiv. **License:** CC BY-NC-ND 4.0

1. INTRODUCTION

The emergence of shape is a fascinating feature of living matter[1,2]. In a synthetic setting, also a wide diversity of solid structures with "life-like" appearances can be created via relatively simple experimental protocols. Examples include polycrystalline biomorphic shapes such as micro flowers[3–7], corals and helices that form via coupled precipitation reactions; "chemical gardens" that emerge from combinations of reaction-diffusion, convection and precipitation[8,9], and electrochemically grown dendrites with fractal branches[10,11] that resemble geometries found in trees, fungi networks and neurons. Applications of such matter ranges from optical waveguides[12] to micropatterned materials[13] to neuromorphic circuitry[14,15].

The bottom-up formation of structure strongly relies on a fine balance over physico-chemical gradients that guide positioning of the chemical building blocks throughout the growth process[16]. Such self-organization does not require dedicated (e.g. lithographic) instrumentation for top-down manipulation, but critically relies on control over the interplay of reaction, diffusion and gradients involved. Molecular and supramolecular systems enable a wide diversity of strategies to direct the growth of solid structures[17]. Self-assembled monolayers or proteins have been used to template crystallization[18–21]; 1D supramolecular assemblies to cast nanowires from metals or inorganic material[22–28]; (supra)molecular ligands or DNA strands to couple nanoparticles into materials[29–32] or functional nanocavities[33,34], and proteins to catalyse the metallization of nanowires amongst electrodes in neuromorphic circuits[35]. Furthermore, hydrogels and viscous polymer solutions have been exploited to modulate diffusion, reaction or crystallization dynamics, and thereby generate structured hybrid materials[36–39].

Here, we establish a dynamic molecular system that exploits the growth of myelin assemblies floating over an aqueous medium to guide the electrodeposition of copper dendrites by the transport of copper(II) (Cu^{2+}) ions. Without the guiding element, the reduction of copper(II) from an aqueous solution results in a radial growth of dendritic structures from the surface of the cathode[40–45]. Due to their conductivity, these wires are repelled from the negative electrode and grow towards the Cu^{2+}-rich medium upon electrodeposition at their tips – a combination of reaction, diffusion and electrostatics that provides these so-called dendrites with a fractal-like morphology. We reasoned that the growth of these copper-based dendrites can be directed by soft and dynamic assemblies that locally release Cu^{2+}. To this end, we employ myelins assembled from the amphiphile triethyleneglycol monododecyl ether ($C_{12}E_3$), loaded with Cu^{2+}. Earlier, we demonstrated how $C_{12}E_3$ forms a lamellar phase of closely packed bilayers at the boundary of a $C_{12}E_3$ droplet when deposited at an air-water interface[46,47]. Swelling of the bilayer phase upon uptake of water drives the growth of multilamellar myelin filaments from the droplet[48,49], which spread over the air-water interface. The concomitant release of individual $C_{12}E_3$ amphiphiles as a surfactant to the air-water interface generates outbound Marangoni flows which extrude myelins from the $C_{12}E_3$ droplet[50]. Thereby, Cu^{2+}-loaded myelins are anticipated to create localized Cu^{2+} gradients that direct the structures obtained upon copper electrodeposition.

As the building blocks for our system, we first study the growth of $C_{12}E_3$-based myelins loaded with Cu^{2+} ions in the interior of the lamellar phase. Second, we assess the growth of copper dendrites via electrodeposition under sub-mM conditions – matching the concentration levels of Cu^{2+} anticipated upon release from the myelins. Third, we show how the myelins deliver Cu^{2+} ions at the growing tips of the copper dendrites, and thereby direct the path of electrodeposited connections grown in the system. Finally, we explore the potential of the Cu^{2+}-loaded myelins to establish dynamic, reconfigurable connections stemming from a central $C_{12}E_3$ droplet towards multiple electrodes – a first step towards hyperconnected networks of electrodeposited wires.

https://doi.org/10.26434/chemrxiv-2024-qhmqn ORCID: https://orcid.org/0000-0002-3395-7197 Content not peer-reviewed by ChemRxiv. License: CC BY-NC-ND 4.0

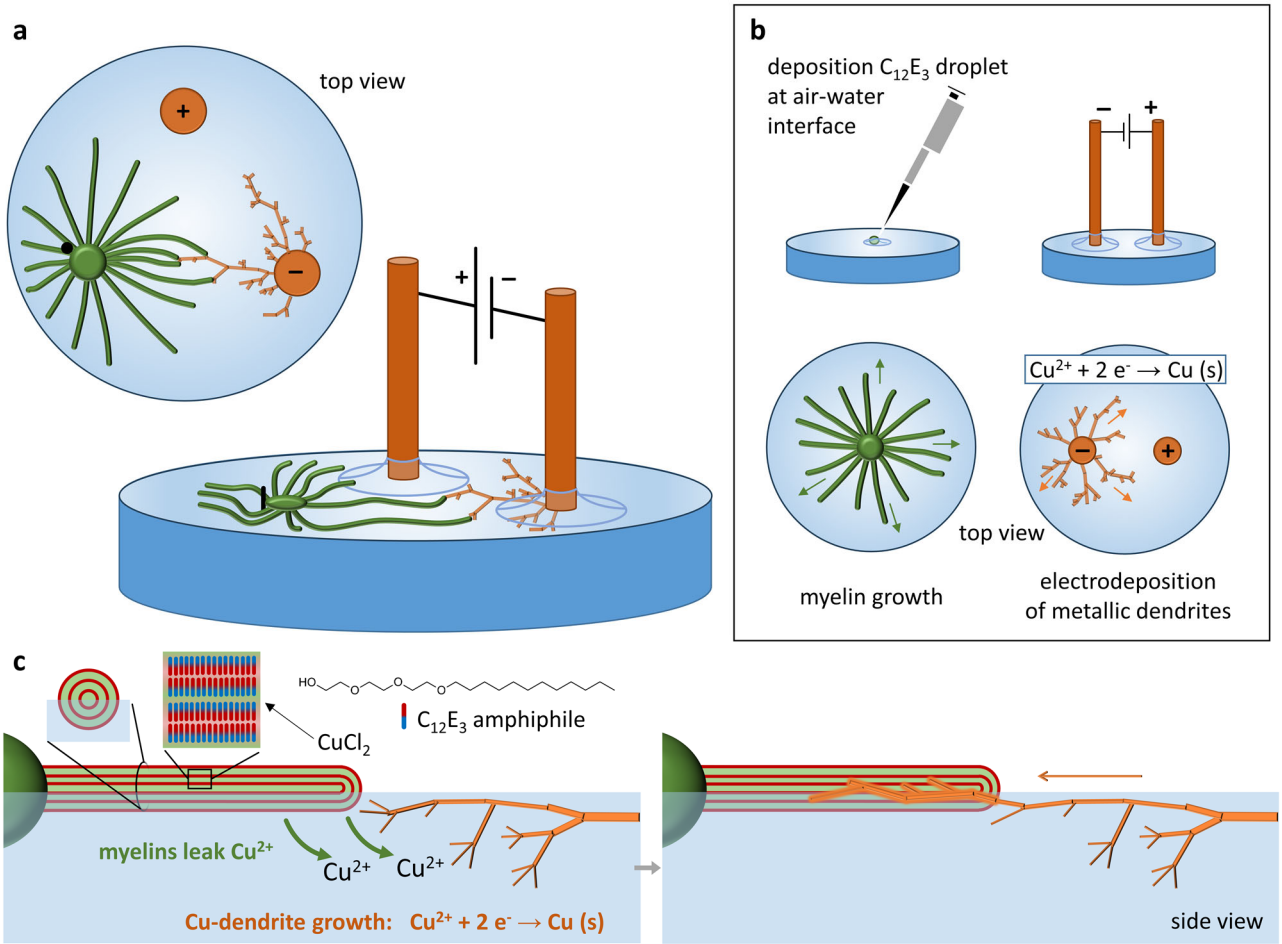

Figure 1. Myelin filaments shaping the electrodeposition of copper dendrites at air-water interfaces. **a)** Schematic representation of myelin assemblies (green) that grow over an air-water interface and deliver copper(II) (Cu^{2+}) ions, which are electrodeposited upon reduction and result into copper dendrites that grow from a negative electrode. **b)** As building blocks of our system, we exploit 1) myelin filaments, growing from a droplet of $C_{12}E_3$ amphiphiles when deposited at the air-water interface; and 2) the dendritic, fractal structures that grow from the surface of a negative electrode when placed in a solution of Cu^{2+} ions, via the reaction $Cu^{2+} + 2\ e^- \rightarrow Cu\ (s)$. **c)** When a copper(II) salt is loaded in the bilayer structure of the $C_{12}E_3$-based myelins, Cu^{2+} leaks from the myelins in the surrounding aqueous solution, and thereby creates a Cu^{2+} gradient that directs the growth of the copper dendrites upon electrodeposition – ultimately allowing the dendrites to grow along the Cu^{2+}-loaded myelins.

https://doi.org/10.26434/chemrxiv-2024-qhmqn **ORCID:** https://orcid.org/0000-0002-3395-7197 Content not peer-reviewed by ChemRxiv. **License:** CC BY-NC-ND 4.0

2. RESULTS AND DISCUSSION

2.1. Growth of Amphiphile Myelins Loaded with Cu^{2+} Ions.

To grow myelins that are loaded with copper(II) ions, we first mix copper(II)chloride ($CuCl_2$) with the $C_{12}E_3$ amphiphile. At a molar ratio of 18.5% (*i.e.* $CuCl_2/C_{12}E_3$ 0.185 mol / 1.00 mol) we observed the $CuCl_2$ salt to be entirely dispersed in the liquid $C_{12}E_3$ phase, and the $CuCl_2/C_{12}E_3$ mixture forms a homogeneous liquid phase with a green/yellow colour (Figure S1). We test the filament growth by depositing $CuCl_2/C_{12}E_3$ "source" droplets (1 μL) on water (5.5 mL, 38 mm diameter Petri dish) with traces of $C_{12}E_3$ at the interface (Figure 2a-b). As shown in Figure 2c-d, myelins grow from the source droplet – comparable to results obtained with $C_{12}E_3$-based droplets we reported earlier[47,50,51]. Furthermore, after deposition, the $CuCl_2/C_{12}E_3$ droplets show a gradual colour change from dark yellow-green to clear blue, starting from the boundary of the droplet and penetrating to the core over a time course of 2 min (Figure 2e, Movie 1). As copper(II) solutions in water are typically blue, even at high concentration, this colour change is indicative of the hydration of copper(II) ions upon water intake amongst the amphiphile bilayers that is inherent to the myelin formation.

Inclusion of $CuCl_2$ affects the myelin growth, although their final length (up to 3 mm, Figure S1) is comparable to myelins grown from pure $C_{12}E_3$ source droplets. We observe the formation of spheroids at the tips of the myelins, as well as pearling along the thinnest ones (Figure 2d). These morphological features do not occur in the absence of Cu^{2+} (Figure S1), and we hypothesize that those are related to an enhanced interfacial tension of the myelin-water interface due to interaction of Cu^{2+} and $C_{12}E_3$. Therefore, we conclude that upon myelin growth from the Cu^{2+}-loaded $C_{12}E_3$ droplet, the Cu^{2+} ions are at least partly residing in the lamellar phase of the myelin. At the same time, however, Cu^{2+} ions are released to the surrounding aqueous phase, giving an enhanced conductivity of the aqueous solution (*vide infra*). Together, our results show the growth of Cu^{2+}-loaded myelins, from which release of Cu^{2+} ions potentially allows for directed electrodeposition of copper dendrites.

https://doi.org/10.26434/chemrxiv-2024-qhmqn ORCID: https://orcid.org/0000-0002-3395-7197 Content not peer-reviewed by ChemRxiv. License: CC BY-NC-ND 4.0

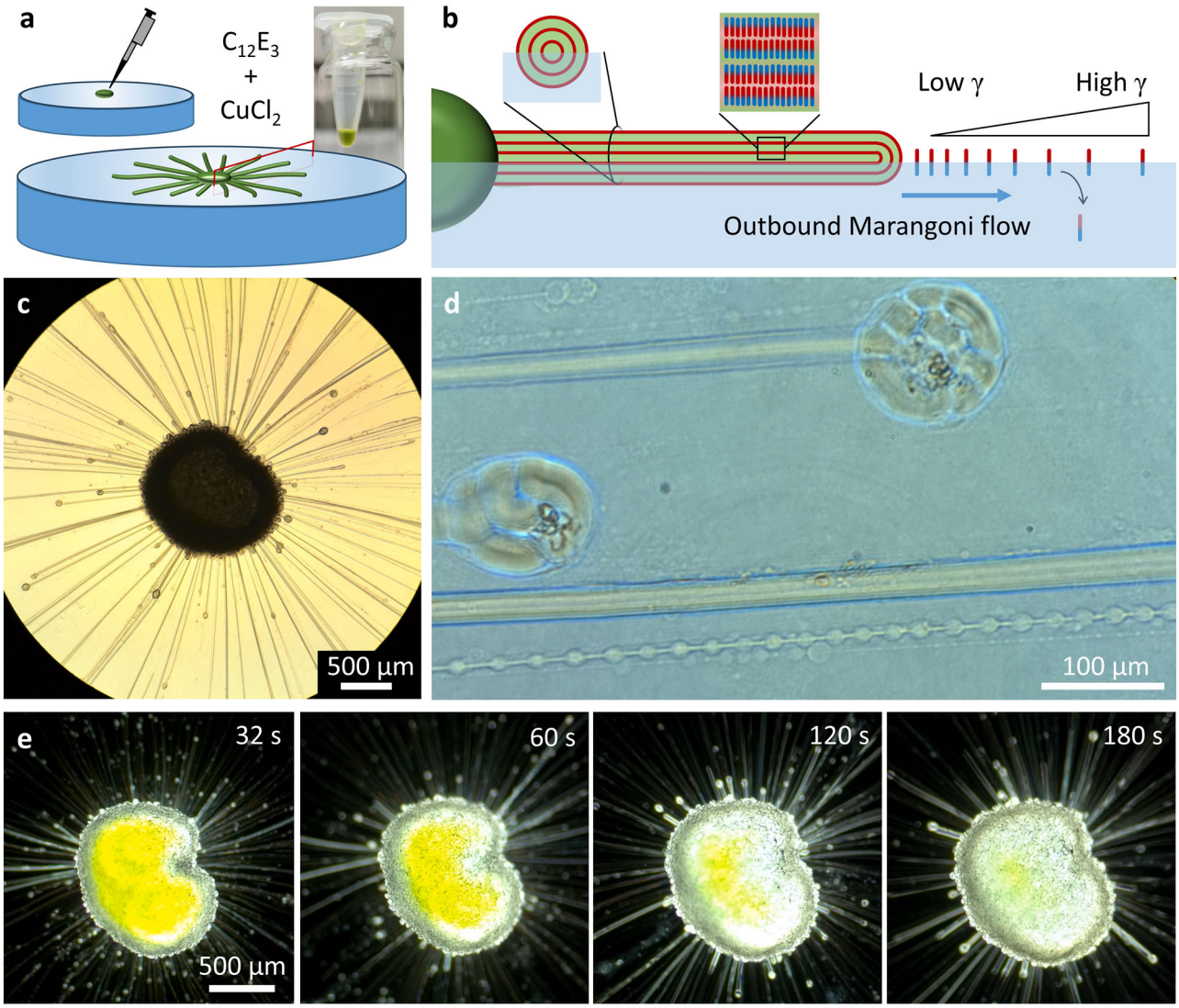

Figure 2. Growth of $C_{12}E_3$-based myelins loaded with $CuCl_2$ over the air-water interface. **a)** Myelins grow from a microliter $CuCl_2/C_{12}E_3$ source droplet, a green/yellow liquid as shown in the photograph of the Eppendorf, when deposited at the interface of MQ water. **b)** The myelin growth is driven by the release of $C_{12}E_3$ surfactants to the air/water interface, which subsequently dissolve in the underlying aqueous solution, generating a surface tension gradient that drives an outbound Marangoni flow along the air-water interface that extrudes the myelins from the droplet. **c)** Optical microscopy image of the myelins, growing from the source droplet in the center. **d)** The inclusion of $CuCl_2$ (16.7 mol%)affects the myelin structure, generating spheroids at their tips, whereas the thinnest myelins show pearling. **e)** Optical microscopy recording of the infusion of water into the $CuCl_2$-loaded source droplet, displaying a colour change from green-yellow to light blue, indicative of copper(II) hydration. **[→ Movie 1]**

https://doi.org/10.26434/chemrxiv-2024-qhmqn **ORCID:** https://orcid.org/0000-0002-3395-7197 Content not peer-reviewed by ChemRxiv. **License:** CC BY-NC-ND 4.0

2.2. Electrochemical Growth of Copper Dendrites.

We anticipated that the release of Cu^{2+} from our myelins results in sub-mM concentrations of the copper(II) supply for the growth of the dendrites. For example, with a 2 µL source droplet containing 18.5 mol% $CuCl_2$, the upper limit to the copper(II) concentration, upon complete release of Cu^{2+} to the aqueous phase, equals 200 µM. This concentration is well below the copper(II) concentrations that are typically used for electrodeposition studies of dense copper fractals[43–45]. Therefore, we first study the electrochemical deposition of copper dendrites from aqueous $CuCl_2$ solutions with concentrations between 10 µM and 1 mM.

We used an electrochemical workstation connected to two copper rods, respectively the working (-) and counter (+) electrode, and a platinum wire as pseudo reference. The electrodes are dipped approx. 1 mm in the aqueous $CuCl_2$ solution, such that the copper dendrites that grow from the negative electrode stay close to the air-water interface (Figure 3a). By applying a potential of -8 V at the working electrode, dendrite growth is followed over time in optical microscopy (Movie 2). Figure 3b shows how more abundant and denser dendritic structures grow from the working electrode with increasing copper(II) concentration in the aqueous solution. With 10 µM $CuCl_2$, no dendrites were obtained even after 20 minutes, whereas all solutions with higher $CuCl_2$ concentrations (50 µM and higher) did result in dendrite growth, suggesting a threshold concentration required for the nucleation of the dendrites. In Figure 3f, we follow the formation of the copper dendrites over time with a solution of 100 µM $CuCl_2$. Up to t = 120 s, only tiny structures grow from the electrode surface, whereas around t = 150 s, the first elongated dendrite forms, marked by a sharp increase in the average dendrite length L vs time (Figure 3d). Such a lag time in the growth of these elongated dendrites only occurs at intermediate $CuCl_2$ concentrations of 50 – 200 µM: At higher concentrations, the dendrites grow steadily into more densely packed structures directly when the voltage is applied (Movie 2). For example, with 1 mM $CuCl_2$, the average length L of the deposited structures increases directly at $t = 0$, without a lag time (Figure 3d). Furthermore, right from the onset of their growth, these structures are more densely packed in comparison to the dendrites obtained at lower concentrations, as is evidenced by their higher fractal dimension D that we obtained using the *''Fractal Box Count''* plug-in in ImageJ (Figure 3e)[52].

Importantly, no bubbles were observed at the electrodes, which indicates that, rather than splitting water, all electrons delivered at the working electrode are involved in the electrodeposition of copper (*i.e.* Cu^{2+} (aq) + 2 e^- → Cu (s)). The average current intensity increases linearly with the initial $CuCl_2$ concentration (Figure 3c), which implies that also the rate of copper deposition is proportional to the availability of Cu^{2+} ions in the aqueous solution. The copper deposition (m, in mol) can be estimated based on the current intensity $I(t)$ via $m = \frac{1}{zF}\int_0^t I(t)dt$, with $z = 2$ and Faraday constant $F = 96485$ C mol^{-1}. For example, for the dendrites grown from the 100 µM $CuCl_2$ solution, the copper deposition equals approx. $3.1 \cdot 10^{-7}$ mol over a time period of 10 min, which represents 56% of the initial copper(II) amount present in the solution. As the current intensity was observed to stay relatively constant (Figure S2), this implies that the deposited Cu^{2+} ions are replaced by new Cu^{2+} ions formed upon oxidation at the copper counter electrode.

https://doi.org/10.26434/chemrxiv-2024-qhmqn ORCID: https://orcid.org/0000-0002-3395-7197 Content not peer-reviewed by ChemRxiv. License: CC BY-NC-ND 4.0

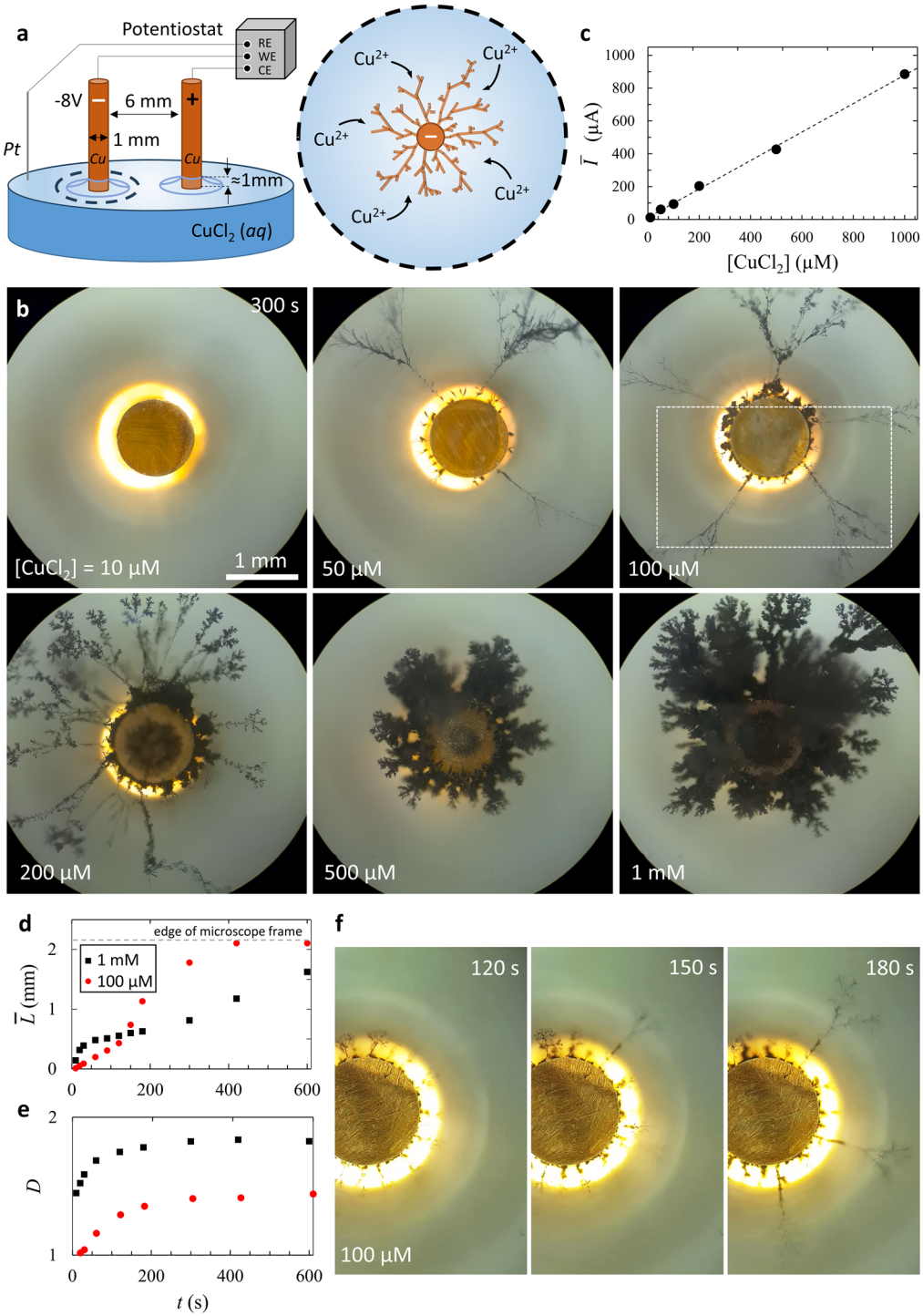

Figure 3. Characterization of copper dendrite growth from $CuCl_2$ solutions in the sub-mM concentration regime. **a)** Schematic representation of the electrochemical cell, comprising two copper electrodes placed in an aqueous $CuCl_2$ solution, and connected to a Pt-wire referenced potentiostat that applies a potential of -8 V to the working electrode. As Cu^{2+} ions are electrodeposited at the negative working electrode, fractal copper dendrites grow from the surface of the electrode towards the surrounding aqueous solution. **b)** Optical microscopy images of copper dendrites grown over a time period of 300 s from the negative electrode, from solutions with a starting $CuCl_2$ concentration ranging from 10 μM to 1 mM. **c)** Average current I during the electrodeposition vs starting $CuCl_2$ concentration in the aqueous solution. **d)** Time-dependent average length L, measured from the surface of the electrode, of copper dendrites that are electrodeposited from $CuCl_2$ solutions of 100 μM and 1 mM. **e)** Time-dependent fractal dimension D of copper dendrites that are electrodeposited from $CuCl_2$ solutions of 100 μM and 1 mM. **f)** Optical microscopy images showing the time-dependent development of the copper dendrites growing from a 100 μM $CuCl_2$ solution. The field of view corresponds to the dashed white box in pane b). To improve the visibility of the dendrites in the onset of their growth, the contrast of the images in f) is enhanced. **[→ Movie 2]**

https://doi.org/10.26434/chemrxiv-2024-qhmqn ORCID: https://orcid.org/0000-0002-3395-7197 Content not peer-reviewed by ChemRxiv. License: CC BY-NC-ND 4.0

2.3. Myelins Guiding the Copper Dendrite Growth.

To study the interaction between the copper-loaded myelins and the dendrites that grow from the working electrode, we introduce a $C_{12}E_3$ source droplet with $CuCl_2$ (16.7 mol%) in the electrochemical cell, as shown in Figure 4a and Movie 3. The source droplet is kept in position by tethering it to the meniscus of a metal pin, using the "Cheerios" effect[53]. When a potential of -8 V is applied, copper dendrites grow from the working electrode within 30 seconds, and tether to the myelins that grow in the direction of the electrode. Upon touching the myelins, the dendrites grow along them by consuming the copper(II) these structures contain (Figure. 4d and Movie 3). Thereby, after 90 s, the dendrites span a distance up to 3.5 mm from the electrode (Figure 4b), featuring a much faster growth compared to the electrodeposition in the absence of the myelins (Figure 3). In the early stages of the growth process, the connection of dendrites and myelins appears to be fragile: some dendrites are pushed away from the source droplet due to the outbound Marangoni flow; disconnect from the myelins or break from their contact point at the electrode. Over time however, copper dendrites reach the source droplet while following the filaments (t = 464 s). Next, electrodeposition of copper starts off inside the source droplet, which transforms the appearance of the source droplet in optical microscopy from yellow to black (Figure 4c). After the dendrites have reached the source droplet, the electrodeposited connection amongst the working electrode and the source becomes more stable and less sensitive to disturbing Marangoni flows (Movie 3).

https://doi.org/10.26434/chemrxiv-2024-qhmqn **ORCID:** https://orcid.org/0000-0002-3395-7197 Content not peer-reviewed by ChemRxiv. **License:** CC BY-NC-ND 4.0

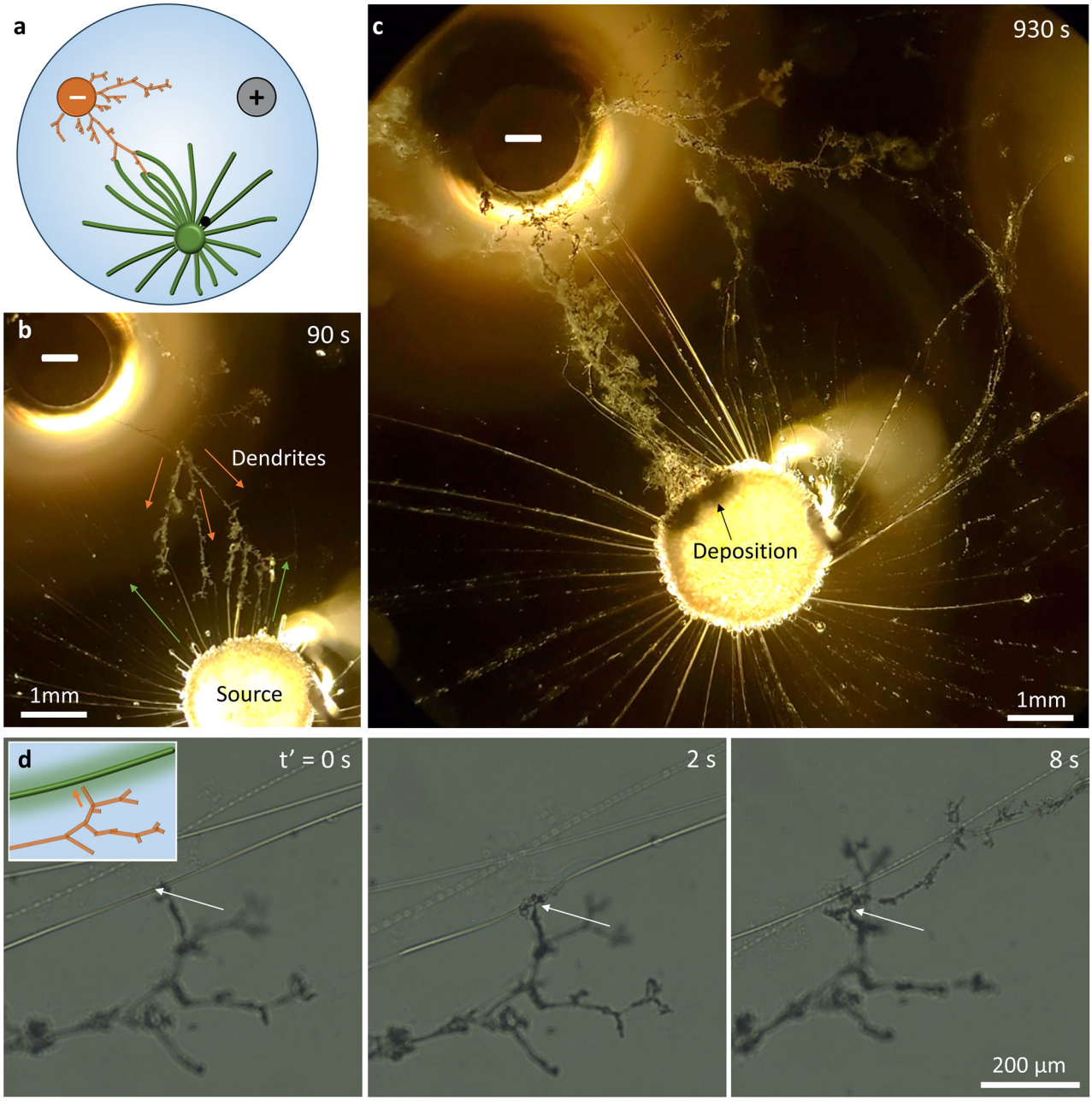

Figure 4. Probing the interaction between the copper dendrites and the Cu^{2+}-loaded myelins. **a)** Schematic representation of the experiment: In an electrochemical cell as shown in Figure 3a with a copper working electrode and a glassy carbon counter electrode, a source droplet loaded with $CuCl_2$ (16.7 mol%) was placed at the air-water interface and kept in place by the meniscus of a metal pin in the solution. Next, a voltage of -8 V was applied. **b)** Optical microscopy image of copper dendrites (orange arrows) growing from the working electrode and interacting with the myelins (green arrows) growing from the source. **c)** The dendrites ultimately reach the source droplet and electrodeposition of copper starts off inside the source droplet. **d)** High magnification optical microscopy recording of copper dendrites that interact and grow along the copper-loaded myelins. **[→ Movie 3]**

https://doi.org/10.26434/chemrxiv-2024-qhmqn **ORCID:** https://orcid.org/0000-0002-3395-7197 Content not peer-reviewed by ChemRxiv. **License:** CC BY-NC-ND 4.0

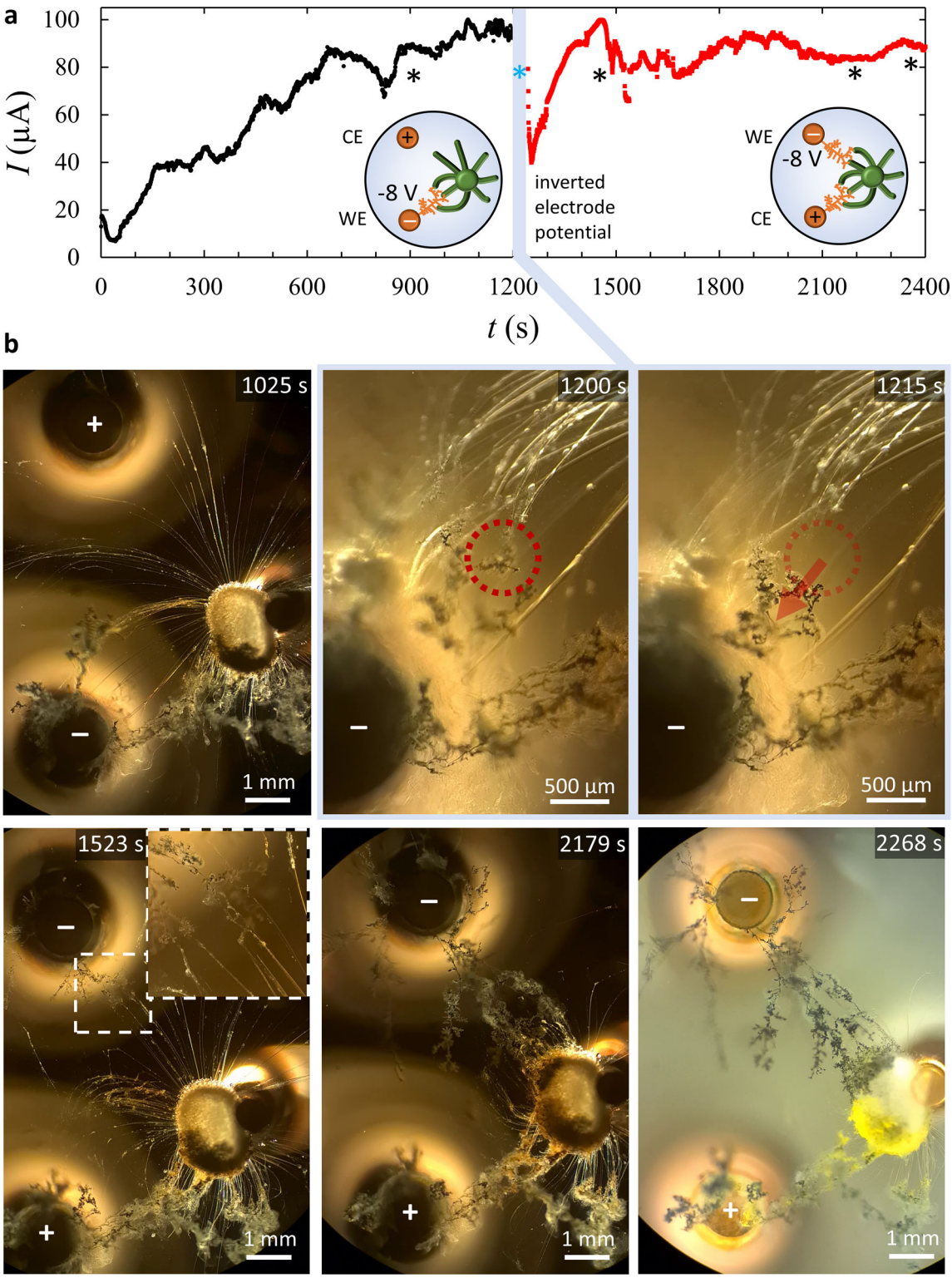

Figure 5. Probing the current involved in the electrodeposition of copper dendrites along Cu^{2+}-loaded myelins. **a)** Current *I* vs time for an electrochemical cell as shown in Figure 3a with two copper electrodes, and a copper-loaded source droplet (1.0 μL, 16.7 mol% $CuCl_2$) placed on MQ water. First, a voltage of -8 V was applied to the working electrode (bottom), and at t = 1200 s, the potential to the electrodes was inverted, such that the top electrode became the working electrode. **b)** Optical microscopy images acquired at different time points, featuring the electrodeposition of copper dendrites in the source droplet (1025 s); the sudden loss of interaction between dendrites and myelins when the potential is turned off (1200 s vs 1215 s); the growth of new dendrites from the top electrode when a negative voltage is applied (1523 s), followed by electrodeposition from this electrode in the source droplet (2179 s), and the color differences between the dendrites electrodeposited in the two cycles, shown in bright field microscopy (2268 s). **[→ Movie 4]**

https://doi.org/10.26434/chemrxiv-2024-qhmqn ORCID: https://orcid.org/0000-0002-3395-7197 Content not peer-reviewed by ChemRxiv. License: CC BY-NC-ND 4.0

To further unravel the interaction between the dendrites and the myelins, we probe the current over time while following the electrodeposition with optical microscopy – using a similar experimental setup as shown in Figure 4a with two copper electrodes (Figure 5a and Movie 4). Right after deposition of the $CuCl_2$-loaded source droplet, a voltage of -8 V is applied at the working electrode, generating a current of approx. 20 µA. This current is well above the conductivity obtained with pure MQ water in the same setup (2.6 µA, Figure S2) and indicative of ions being released from the source droplet to the aqueous solution. Over a time course of approx. 100 s, the current first decreases and then increases at t = 55 s, concomitant with the sudden growth of a single dendrite branch from the working electrode that establishes the first connections with the myelins. As the dendrites grow and interact with the myelins, the current steadily increases. At t = 450 s, the first dendrites that followed the myelins reach the source droplet, where electrodeposition of copper starts. Around t = 900 s, the current levels off at approx. 100 µA, resembling the current intensities that were obtained when depositing copper dendrites from a 100 µM $CuCl_2$ solution (Figure 3c and Figure S2). However, whereas the current during electrodeposition of copper dendrites from a homogeneous 100 µM $CuCl_2$ solution was observed to stay relatively constant (Figure S2), during the electrodeposition of dendrites that grow from Cu^{2+} ions delivered by the myelins, the current increases from approx. 20 µA to 100 µA (Figure 5a). This increasing current indicates that the rate of electrodeposition increases over time, as the dendrites establish more connections with the myelins – and ultimately the source droplet – that provide the copper(II) supply at localized, high concentrations (t = 450 s).

We assessed the reversibility of the connections that are formed upon electrodeposition by inverting the potentials applied to the two electrodes at t = 1200 s. Immediately after a negative potential of -8V is applied to the new working electrode, the current drops to 40 µA, but it rises again, as dendrites nucleate from this electrode and connect to the myelins. Again, the dendrites reach the source droplet as they grow along the myelins at t = 1800 s, and the current levels off at approx. 85 µA. Importantly, this current intensity implies that the electrodeposited dendrites do not establish a conductive pathway via the source droplet that connects both electrodes. Indeed, bright field optical microscopy images reveal that the dendrites as well as the electrodeposited material in the source droplet that have been formed in the time period [0 – 1200] s have turned (in part) yellow (Figure 5b). This suggests the oxidation of copper while these structures were in contact with the positive electrode in the time period [1200 – 2400] s.

Together, our results show that the dendrites have a strong preference to grow towards the myelins and source droplet, as their main supply of Cu^{2+} ions. Furthermore, a negative potential is required to sustain the electrodeposited structures. Despite partly oxidation, which can already take place when exposed to a negative potential[40], the conductive nature of the copper dendrites is demonstrated by their repulsion from the working electrode, and their mutual repulsion as they continuously move to avoid each other (Figure 3 and Movie 2). We reason that these repulsion effects cause the dendrites to spread out, which, in turn, enhances their chance to encounter a myelin at the air-water interface, grow along the Cu^{2+} gradient towards the myelin and consume the Cu^{2+} carried by the myelin. At the same time, the interaction with the myelins keeps the high-density copper dendrites afloat at the air-water interface. For example, we note that when switching the potential from -8 V to 0 V at t = 1200 s, the dendrites that were growing from the working electrode and tethering to the myelins instantly detached from these myelins, as they relaxed backwards to the electrode and also sank from the air-water interface (Figure 5b and Movie 4). In contrast, the dendrites that were connected to the source droplet and therefore more embedded in supportive myelin structures remained present at the air-water interface.

https://doi.org/10.26434/chemrxiv-2024-qhmqn ORCID: https://orcid.org/0000-0002-3395-7197 Content not peer-reviewed by ChemRxiv. License: CC BY-NC-ND 4.0

2.4. Reconfigurable Connections in Electrodeposited Networks.

We explore how the copper-loaded myelins allow for the growth of multiple connections, generating dynamic and hyperconnected networks of electrodeposited wires. First, we assessed the connections growing via electrodeposition when a source droplet was placed amongst 6 copper electrodes positioned in a hexagonal array, as shown in Figure 6a (and figure S4 for details of the setup). With 3 electrodes as working electrode (-8 V) and 3 electrodes as counter electrode, we observe that the dendrites grow along the myelins, reaching the source at approx. 3 min and maintaining the network over a time course of 15 minutes during which the voltage was applied. Even though the dendrites growing from all 3 electrodes do interact with the myelins – establishing a connection from electrode to source, not all dendrites grow up to the source droplet itself. We ascribe the non-directed growth of dendrites to the copper gradients produced upon Cu^{2+} release from the neighbouring counter electrodes. Importantly, the established connections can be reconfigured as upon inverting the applied potential to the electrodes at t = 15 minutes, new dendrites grow from the new working electrodes and start to connect with the myelins, whereas the old dendrites degrade and are removed due to the outbound Marangoni flow from the source droplet. After 15 minutes, comparable behavior was observed for a third cycle of switching the applied potential to the electrodes, again over a time course of 15 minutes. In subsequent cycles, myelin growth was observed to decline, and the dendrites failed to interact with the myelins that were left. We hypothesize that at this point, most Cu^{2+} ions have leaked from the source and the myelins to the aqueous solution, such that the dendrites cannot grow along a Cu^{2+} gradient towards the remaining myelins anymore.

Second, to direct the growth of the dendrites from the electrodes towards the source droplet, we positioned the copper counter electrode in the source droplet, which is placed inside the hexagonal array of electrodes. We reasoned that both the electric field and the Cu^{2+} gradient produced by the central counter electrode further guides the growth of the dendrites towards the central source. Indeed, we observe that when the potential (-8 V) is applied as shown in Figure 6b, dendrites growing from all the 3 working electrodes have already reached the source droplet after 60 s, and after 2 minutes, the connections from the electrodes are reinforced with multiple paths connecting to the source droplet. We note that after 5 minutes, the source droplet starts to swell, presumably due to the production of Cu^{2+} ions or other side reactions happening at the counter electrode, which disrupts the connection of the dendrites to the source droplet.

https://doi.org/10.26434/chemrxiv-2024-qhmqn **ORCID:** https://orcid.org/0000-0002-3395-7197 Content not peer-reviewed by ChemRxiv. **License:** CC BY-NC-ND 4.0

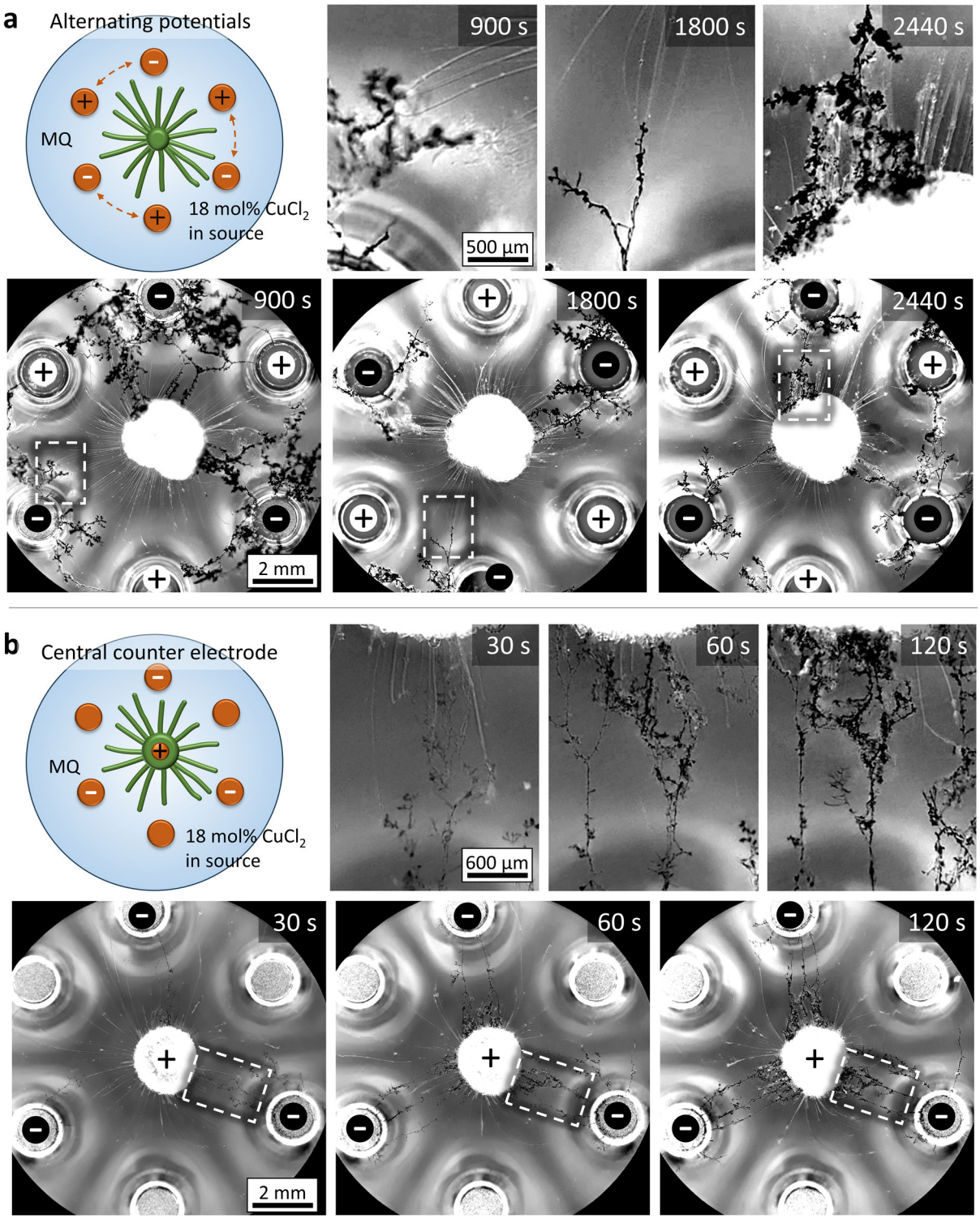

Figure 6. Multiple connections amongst electrodes and source droplet upon electrodeposition. **a)** A copper-loaded source droplet (2.0 µL, 18.5 mol%) is positioned amongst 6 copper electrodes in a hexagonal array on MQ water. The source is kept in position via a copper wire inserted in the droplet. The optical microscopy images feature 3 cycles where in an alternating fashion 3 electrodes are the working electrode (-8 V) and 3 electrodes are the counter electrode. As the potential to the electrodes is switched, we observe the old dendrites to decline, and new dendrites to grow from the 3 working electrodes while interacting with the copper-loaded myelins, some of which reaching the central source droplet. **b)** A copper-loaded source droplet (2.0 µL, 18.5 mol%) is positioned amongst 6 copper electrodes in a hexagonal array on MQ water. A copper wire is inserted in the source droplet. When a voltage of -8 V is applied to 3 working electrodes, and the copper wire inserted in the source droplet functions as counter electrode, dendrites grow rapidly towards the source. To improve the visibility of the myelins (20-80 µm diameter) in the bright field optical microscopy images, the image is converted to grayscale and the contrast is enhanced. **[→ Movie 5]**

https://doi.org/10.26434/chemrxiv-2024-qhmqn **ORCID:** https://orcid.org/0000-0002-3395-7197 Content not peer-reviewed by ChemRxiv. **License:** CC BY-NC-ND 4.0

In a third approach, to avoid the release of copper from the counter electrodes, we used gold plated electrodes to grow dendrites and connect them with a copper-loaded source droplet. However, when a potential of -8 V is applied to the 3 working electrodes, bubbles form at the working electrodes, typical for water splitting taking place as a side reaction to the intended Cu^{2+} electrodeposition (Figure S4). In these experiments we observed that typically the dendrites of only one of the 3 working electrodes reach the source, featuring a 'winner-takes-all' scenario: When the first dendrites reach the droplet, the dendrites growing form the "competing" electrodes gradually decline. We ascribe this decline of dendrites to the depletion of copper in the medium. It is possible that the absence of background Cu^{2+} ions, in previous experiments maintained by the oxidation of the copper-based counter electrodes, now hampers the dendrites to be sustained. Once a first conductive connection from electrode to source droplet has been established, electrodeposition can take place more easily via this path-of-least-resistance towards the Cu^{2+}-rich source droplet, rather than via the dendrites that are only in contact with the Cu^{2+}-poor aqueous medium.

Finally, we establish directional and reconfigurable connections amongst the electrodes and source droplet, while relying exclusively on the Cu^{2+} gradient produced by the myelins. To this end, we placed a copper-loaded source droplet amongst 6 gold plated electrodes in a hexagonal array (Figure 7). With 3 constant counter electrodes, and a current limited to 200 µA to suppress bubble formation, we observe that alternating between different working electrodes – one at a time – allows growing dendrites consistently on demand from a specific electrode. In these conditions, we can create connections between a selected electrode and the source droplet. The connection takes between 1 and 2 minutes to form and features a strong directional character with minimal growth towards the counter electrodes. Furthermore, as the dendrites grow up-stream to the outbound Marangoni flow from the source droplet, previously grown dendrites stemming from inactive electrodes are pushed away. Thereby, the Marangoni flow clears the path for myelins to create a new favourable path for the dendrites to grow towards the source when another electrode is activated.

https://doi.org/10.26434/chemrxiv-2024-qhmqn **ORCID:** https://orcid.org/0000-0002-3395-7197 Content not peer-reviewed by ChemRxiv. **License:** CC BY-NC-ND 4.0

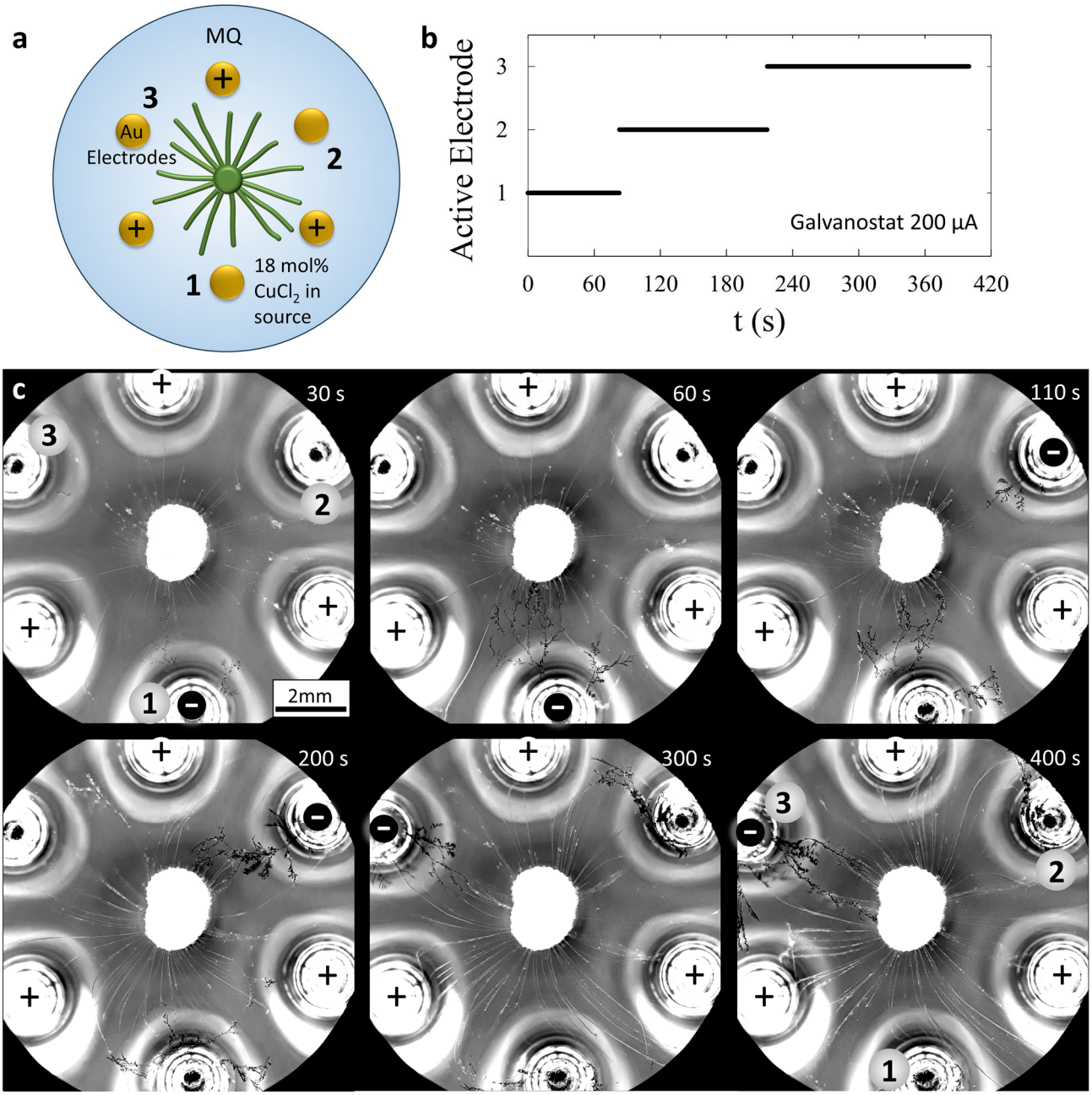

Figure 7. Dynamic, reconfigurable connections amongst electrodes and source droplet. **a)** A copper-loaded source droplet (2 µL, 18.5 mol%) is positioned amongst 6 gold plated electrodes in a hexagonal array on MQ water. The source is kept in position via a copper wire inserted in the droplet. 3 electrodes function as counter electrode, as indicated in the scheme, and the working electrode alternates from position 1, 2 and 3 over time, as indicated in **b). c)** Optical microscopy images featuring the dendrites that grow from the active working electrode, while the old dendrites from electrodes that are no longer active decline and get pushed away from the source droplet by the Marangoni flow. To improve the visibility of the myelins (20-80 µm diameter) in the bright field optical microscopy images, the image is converted to grayscale and the contrast is enhanced. **[→ Movie 6]**

https://doi.org/10.26434/chemrxiv-2024-qhmqn **ORCID:** https://orcid.org/0000-0002-3395-7197 Content not peer-reviewed by ChemRxiv. **License:** CC BY-NC-ND 4.0

3. CONCLUSIONS

We demonstrate a unique interaction between myelin assemblies that deliver copper(II) ions to the tips of copper dendrites, which in turn grow along the Cu^{2+}gradient upon electrodeposition. First, we succesfully include Cu^{2+} ions amongst the amphiphile bilayers in the myelins, which grow out from a surfactant droplet over an air-water interface. Next, we show how the myelins deliver Cu^{2+} at a negative electrode placed in solution, allowing copper dendrites to grow upon electrodeposition. Intriguingly, the growing copper dendrites follow the Cu^{2+} gradient towards the myelins, and grow along the Cu^{2+} containing myelins towards the surfactant droplet – displaying a unique interplay between molecular assemblies and inorganic, solid structures. We exploit the system to establish reconfigurable connections amongst electrodes and surfactant droplets via Cu^{2+}-loaded myelins that template the copper electrodeposition. We note that our approach – even though based on a simpler system – bears an intriguing analogy with the build-up of biominerals in giant marine cells. In *Amphistegina lobifera*, it has been shown how vesicles supply ions, loaded upon endocytosis of sea water, to the calcification site[54].

We envision that bottom-up assembly of (semi)conductive wires enables new routes towards next generations of intelligent materials, in particular with the growing interest in neuromorphic circuitry. In this context, the general applicability of our concept is enhanced by a design that requires only simple and easily accessible molecular building blocks, such as commercially available surfactants, copper(II) salts and metal electrodes. For example, the surfactant assemblies can deliver metal ions, but also EDOT monomers that form semiconductive polyEDOT connections upon electropolymerization[14]. Furthermore, as the templating myelins spread out in all directions from the source droplet, such droplets can function as nodes that are hyperconnected to many electrodes via the electrodeposited wires – bearing an analogy with brain cells.

ASSOCIATED CONTENT

Movie 1: Optical microscopy recording of $CuCl_2/C_{12}E_3$ source droplet deposited on MQ water (MP4).

Movie 2: Optical microscopy recordings of copper dendrite growth from working electrodes placed in aqueous $CuCl_2$ solutions (10 µM to 1 mM) over a time period of 20 minutes (MP4).

Movie 3: Optical microscopy recordings of copper dendrites growing from the copper working electrode (- 8 V) that interact with the Cu^{2+}-loaded myelins growing from the source on MQ water.

Movie 4: Optical microscopy recordings of the interactions of the Cu^{2+}-loaded myelins and the dendrites growing from two different copper electrodes that are consecutively applied as working electrode (-8 V) (MP4).

Movie 5: Optical microscopy recordings of multiple connections established amongst a Cu^{2+}-loaded source droplet placed amongst 6 copper electrodes in a hexagonal array. (MP4)

Movie 6: Optical microscopy recording of dynamic, reconfigurable connections amongst a Cu^{2+}-loaded source droplet placed amongst 6 gold plated electrodes in a hexagonal array. (MP4)

Additional experimental details, materials and methods, supporting figures and descriptions of supporting movies.

https://doi.org/10.26434/chemrxiv-2024-qhmqn ORCID: https://orcid.org/0000-0002-3395-7197 Content not peer-reviewed by ChemRxiv. License: CC BY-NC-ND 4.0

Notes

The authors declare no competing financial interest.

ACKNOWLEDGEMENTS

We thank T. Peters for helpful advice with the potentiostat, and C. Nijhuis, R. Zinelli, I. Lin, M. Winkens, P. de Visser, T. de Jong and W. Huck for stimulating discussions. The authors thank the Dutch Research Council (NWO, ENW-M1 grant no. OCENW.M20.173 and VIDI grant no. VI.Vidi.213.128) as well as the Dutch Ministry of Education, Culture and Science (gravitation program 024.001.035) for financial support.

REFERENCES

(1) Thompson, D. W. *On Growth and Form*; University Press: Cambridge, 1917.

(2) P. Ball. *The Self-Made Tapestry*, 1st ed.; Oxford Univ. Press: Oxford, 1999.

(3) García-Ruiz, J. M.; Hyde, S. T.; Carnerup, A. M.; Christy, A. G.; Van Kranendonk, M. J.; Welham, N. J. Self-Assembled Silica-Carbonate Structures and Detection of Ancient Microfossils. *Science (1979)* **2003**, *302* (5648), 1194–1197. https://doi.org/10.1126/science.1090163.

(4) García-Ruiz, J. M.; Melero-García, E.; Hyde, S. T. Morphogenesis of Self-Assembled Nanocrystalline Materials of Barium Carbonate and Silica. *Science (1979)* **2009**, *323* (5912), 362–365. https://doi.org/10.1126/science.1165349.

(5) Knoll, P.; Nakouzi, E.; Steinbock, O. Mesoscopic Reaction–Diffusion Fronts Control Biomorph Growth. *The Journal of Physical Chemistry C* **2017**, *121* (46), 26133–26138. https://doi.org/10.1021/acs.jpcc.7b09559.

(6) Noorduin, W. L.; Grinthal, A.; Mahadevan, L.; Aizenberg, J. Rationally Designed Complex, Hierarchical Microarchitectures. *Science (1979)* **2013**, *340* (6134), 832–837. https://doi.org/10.1126/science.1234621.

(7) Kaplan, C. N.; Noorduin, W. L.; Li, L.; Sadza, R.; Folkertsma, L.; Aizenberg, J.; Mahadevan, L. Controlled Growth and Form of Precipitating Microsculptures. *Science (1979)* **2017**, *355* (6332), 1395–1399. https://doi.org/10.1126/science.aah6350.

(8) Nakouzi, E.; Steinbock, O. Self-Organization in Precipitation Reactions Far from the Equilibrium. *Sci Adv* **2016**, *2* (8). https://doi.org/10.1126/sciadv.1601144.

(9) Haudin, F.; Cartwright, J. H. E.; Brau, F.; De Wit, A. Spiral Precipitation Patterns in Confined Chemical Gardens. *Proceedings of the National Academy of Sciences* **2014**, *111* (49), 17363–17367. https://doi.org/10.1073/pnas.1409552111.

(10) Kozicki, M. N. Information in Electrodeposited Dendrites. *Adv Phys X* **2021**, *6* (1). https://doi.org/10.1080/23746149.2021.1920846.

(11) Smith, J. H.; Rowland, C.; Harland, B.; Moslehi, S.; Montgomery, R. D.; Schobert, K.; Watterson, W. J.; Dalrymple-Alford, J.; Taylor, R. P. How Neurons Exploit Fractal Geometry to Optimize Their Network Connectivity. *Sci Rep* **2021**, *11* (1), 2332. https://doi.org/10.1038/s41598-021-81421-2.

(12) Helmbrecht, L.; Tan, M.; Röhrich, R.; Bistervels, M. H.; Kessels, B. O.; Koenderink, A. F.; Kahr, B.; Noorduin, W. L. Directed Emission from Self-Assembled Microhelices. *Adv Funct Mater* **2020**, *30* (26). https://doi.org/10.1002/adfm.201908218.

(13) Grzybowski, B. A.; Bishop, K. J. M.; Campbell, C. J.; Fialkowski, M.; Smoukov, S. K. Micro- and Nanotechnology via Reaction–Diffusion. *Soft Matter* **2005**, *1* (2), 114. https://doi.org/10.1039/b501769f.

(14) Cucchi, M.; Kleemann, H.; Tseng, H.; Ciccone, G.; Lee, A.; Pohl, D.; Leo, K. Directed Growth of Dendritic Polymer Networks for Organic Electrochemical Transistors and Artificial Synapses. *Adv Electron Mater* **2021**, *7* (10). https://doi.org/10.1002/aelm.202100586.

https://doi.org/10.26434/chemrxiv-2024-qhmqn **ORCID:** https://orcid.org/0000-0002-3395-7197 Content not peer-reviewed by ChemRxiv. **License:** CC BY-NC-ND 4.0

(15) Cucchi, M.; Gruener, C.; Petrauskas, L.; Steiner, P.; Tseng, H.; Fischer, A.; Penkovsky, B.; Matthus, C.; Birkholz, P.; Kleemann, H.; Leo, K. Reservoir Computing with Biocompatible Organic Electrochemical Networks for Brain-Inspired Biosignal Classification. *Sci Adv* **2021**, *7* (34), eabh0693. https://doi.org/10.1126/sciadv.abh0693.

(16) Nguindjel, A.-D. C.; de Visser, P. J.; Winkens, M.; Korevaar, P. A. Spatial Programming of Self-Organizing Chemical Systems Using Sustained Physicochemical Gradients from Reaction, Diffusion and Hydrodynamics. *Physical Chemistry Chemical Physics* **2022**, *24* (39), 23980–24001. https://doi.org/10.1039/D2CP02542F.

(17) Mann, S. Self-Assembly and Transformation of Hybrid Nano-Objects and Nanostructures under Equilibrium and Non-Equilibrium Conditions. *Nat Mater* **2009**, *8* (10), 781–792. https://doi.org/10.1038/nmat2496.

(18) Aizenberg, J.; Black, A. J.; Whitesides, G. M. Control of Crystal Nucleation by Patterned Self-Assembled Monolayers. *Nature* **1999**, *398* (6727), 495–498. https://doi.org/10.1038/19047.

(19) Davila-Hernandez, F. A.; Jin, B.; Pyles, H.; Zhang, S.; Wang, Z.; Huddy, T. F.; Bera, A. K.; Kang, A.; Chen, C.-L.; De Yoreo, J. J.; Baker, D. Directing Polymorph Specific Calcium Carbonate Formation with de Novo Protein Templates. *Nat Commun* **2023**, *14* (1), 8191. https://doi.org/10.1038/s41467-023-43608-1.

(20) Pouget, E. M.; Bomans, P. H. H.; Goos, J. A. C. M.; Frederik, P. M.; de With, G.; Sommerdijk, N. A. J. M. The Initial Stages of Template-Controlled $CaCO_3$ Formation Revealed by Cryo-TEM. *Science (1979)* **2009**, *323* (5920), 1455–1458. https://doi.org/10.1126/science.1169434.

(21) Mann, S.; Ozin, G. A. Synthesis of Inorganic Materials with Complex Form. *Nature* **1996**, *382* (6589), 313–318. https://doi.org/10.1038/382313a0.

(22) Duxin, N.; Liu, F.; Vali, H.; Eisenberg, A. Cadmium Sulphide Quantum Dots in Morphologically Tunable Triblock Copolymer Aggregates. *J Am Chem Soc* **2005**, *127* (28), 10063–10069. https://doi.org/10.1021/ja0505043.

(23) Sone, E. D.; Zubarev, E. R.; Stupp, S. I. Semiconductor Nanohelices Templated by Supramolecular Ribbons. *Angewandte Chemie International Edition* **2002**, *41* (10), 1705–1709. https://doi.org/10.1002/1521-3773(20020517)41:10<1705::AID-ANIE1705>3.0.CO;2-M.

(24) Reches, M.; Gazit, E. Casting Metal Nanowires Within Discrete Self-Assembled Peptide Nanotubes. *Science (1979)* **2003**, *300* (5619), 625–627. https://doi.org/10.1126/science.1082387.

(25) Wang, H.; Lin, W.; Fritz, K. P.; Scholes, G. D.; Winnik, M. A.; Manners, I. Cylindrical Block Co-Micelles with Spatially Selective Functionalization by Nanoparticles. *J Am Chem Soc* **2007**, *129* (43), 12924–12925. https://doi.org/10.1021/ja075587x.

(26) Seddon, A. M.; Patel, H. M.; Burkett, S. L.; Mann, S. Chiral Templating of Silica-Lipid Lamellar Mesophase with Helical Tubular Architecture. *Angewandte Chemie International Edition* **2002**, *41* (16), 2988. https://doi.org/DOI: 10.1002/1521-3773(20020816)41:16<2988::AID-ANIE2988>3.0.CO;2-3.

(27) Jung, J. H.; Ono, Y.; Hanabusa, K.; Shinkai, S. Creation of Both Right-Handed and Left-Handed Silica Structures by Sol−Gel Transcription of Organogel Fibers Comprised of Chiral Diaminocyclohexane Derivatives. *J Am Chem Soc* **2000**, *122* (20), 5008–5009. https://doi.org/10.1021/ja000449s.

(28) Li, M.; Mann, S. Emergent Hybrid Nanostructures Based on Non-Equilibrium Block Copolymer Self-Assembly. *Angewandte Chemie International Edition* **2008**, *47* (49), 9476–9479. https://doi.org/10.1002/anie.200803231.

(29) Klajn, R.; Bishop, K. J. M.; Fialkowski, M.; Paszewski, M.; Campbell, C. J.; Gray, T. P.; Grzybowski, B. A. Plastic and Moldable Metals by Self-Assembly of Sticky Nanoparticle Aggregates. *Science (1979)* **2007**, *316* (5822), 261–264. https://doi.org/10.1126/science.1139131.

(30) Zhou, W.; Li, Y.; Je, K.; Vo, T.; Lin, H.; Partridge, B. E.; Huang, Z.; Glotzer, S. C.; Mirkin, C. A. Space-Tiled Colloidal Crystals from DNA-Forced Shape-Complementary Polyhedra Pairing. *Science (1979)* **2024**, *383* (6680), 312–319. https://doi.org/10.1126/science.adj1021.

(31) Wang, J.; Peled, T. S.; Klajn, R. Photocleavable Anionic Glues for Light-Responsive Nanoparticle Aggregates. *J Am Chem Soc* **2023**, *145* (7), 4098–4108. https://doi.org/10.1021/jacs.2c11973.

(32) Yee, D. W.; Lee, M. S.; An, J.; Macfarlane, R. J. Reversible Diffusionless Phase Transitions in 3D Nanoparticle Superlattices. *J Am Chem Soc* **2023**, *145* (11), 6051–6056. https://doi.org/10.1021/jacs.3c01286.

https://doi.org/10.26434/chemrxiv-2024-qhmqn **ORCID:** https://orcid.org/0000-0002-3395-7197 Content not peer-reviewed by ChemRxiv. **License:** CC BY-NC-ND 4.0

(33) Bian, T.; Gardin, A.; Gemen, J.; Houben, L.; Perego, C.; Lee, B.; Elad, N.; Chu, Z.; Pavan, G. M.; Klajn, R. Electrostatic Co-Assembly of Nanoparticles with Oppositely Charged Small Molecules into Static and Dynamic Superstructures. *Nat Chem* **2021**, *13* (10), 940–949. https://doi.org/10.1038/s41557-021-00752-9.

(34) Sokołowski, K.; Huang, J.; Földes, T.; McCune, J. A.; Xu, D. D.; de Nijs, B.; Chikkaraddy, R.; Collins, S. M.; Rosta, E.; Baumberg, J. J.; Scherman, O. A. Nanoparticle Surfactants for Kinetically Arrested Photoactive Assemblies to Track Light-Induced Electron Transfer. *Nat Nanotechnol* **2021**, *16* (10), 1121–1129. https://doi.org/10.1038/s41565-021-00949-6.

(35) Fu, T.; Liu, X.; Gao, H.; Ward, J. E.; Liu, X.; Yin, B.; Wang, Z.; Zhuo, Y.; Walker, D. J. F.; Joshua Yang, J.; Chen, J.; Lovley, D. R.; Yao, J. Bioinspired Bio-Voltage Memristors. *Nat Commun* **2020**, *11* (1), 1861. https://doi.org/10.1038/s41467-020-15759-y.

(36) Park, J. H.; Paczesny, J.; Kim, N.; Grzybowski, B. A. Shaping Microcrystals of Metal–Organic Frameworks by Reaction–Diffusion. *Angewandte Chemie International Edition* **2020**, *59* (26), 10301–10305. https://doi.org/10.1002/anie.201910989.

(37) Schroeder, T. B. H.; Aizenberg, J. Patterned Crystal Growth and Heat Wave Generation in Hydrogels. *Nat Commun* **2022**, *13* (1), 259. https://doi.org/10.1038/s41467-021-27505-z.

(38) van Campenhout, C. T.; ten Napel, D. N.; van Hecke, M.; Noorduin, W. L. Rapid Formation of Uniformly Layered Materials by Coupling Reaction–Diffusion Processes with Mechanical Responsiveness. *Proceedings of the National Academy of Sciences* **2022**, *119* (39). https://doi.org/10.1073/pnas.2123156119.

(39) Horváth, J.; Szalai, I.; De Kepper, P. An Experimental Design Method Leading to Chemical Turing Patterns. *Science (1979)* **2009**, *324* (5928), 772–775. https://doi.org/10.1126/science.1169973.

(40) Qi, K.; Huang, H. Electrochemical Migration Behavior of Copper under a Thin Distilled Water Layer. *Corrosion Communications* **2023**, *11*, 52–57. https://doi.org/10.1016/j.corcom.2022.09.004.

(41) Wang, J.; Yi, X.; Zeng, X.; Chen, S.; Wang, R.; Shu, J.; Chen, M.; Xiao, Z. Copper Fractal Growth during Recycling from Waste Printed Circuit Boards by Slurry Electrolysis. *Front Environ Sci Eng* **2021**, *15* (6), 117. https://doi.org/10.1007/s11783-021-1405-7.

(42) Schmädicke, C.; Poetschke, M.; Renner, L. D.; Baraban, L.; Bobeth, M.; Cuniberti, G. Copper Nanowire Synthesis by Directed Electrochemical Nanowire Assembly. *RSC Adv.* **2014**, *4* (86), 46363–46368. https://doi.org/10.1039/C4RA04853A.

(43) Gupta, R.; Ghosh, S.; Choudhury, S.; Ghosh, S. Pattern Transition from Dense Branching Morphology to Fractal for Copper and B′ Brass Electrodeposition in Thin Gap Geometry. *AIP Adv* **2018**, *8* (1). https://doi.org/10.1063/1.5007110.

(44) Ghosh, S.; Gupta, R.; Ghosh, S. Effect of Free Energy Barrier on Pattern Transition in 2D Diffusion Limited Aggregation Morphology of Electrodeposited Copper. *Heliyon* **2018**, *4* (12), e01022. https://doi.org/10.1016/j.heliyon.2018.e01022.

(45) Fleury, V. Branched Fractal Patterns in Non-Equilibrium Electrochemical Deposition from Oscillatory Nucleation and Growth. *Nature* **1997**, *390* (6656), 145–148. https://doi.org/10.1038/36522.

(46) van der Weijden, A.; Winkens, M.; Schoenmakers, S. M. C.; Huck, W. T. S.; Korevaar, P. A. Autonomous Mesoscale Positioning Emerging from Myelin Filament Self-Organization and Marangoni Flows. *Nat Commun* **2020**, *11* (1), 4800. https://doi.org/10.1038/s41467-020-18555-w.

(47) Nguindjel, A.-D. C.; Franssen, S. C. M.; Korevaar, P. A. Reconfigurable Droplet–Droplet Communication Mediated by Photochemical Marangoni Flows. *J Am Chem Soc* **2024**, *146* (9), 6006–6015. https://doi.org/10.1021/jacs.3c12882.

(48) Zou, L.-N.; Nagel, S. R. Stability and Growth of Single Myelin Figures. *Phys Rev Lett* **2006**, *96* (13), 138301. https://doi.org/10.1103/PhysRevLett.96.138301.

(49) Reissig, L.; Fairhurst, D. J.; Leng, J.; Cates, M. E.; Mount, A. R.; Egelhaaf, S. U. Three-Dimensional Structure and Growth of Myelins. *Langmuir* **2010**, *26* (19), 15192–15199. https://doi.org/10.1021/la102726r.

(50) Winkens, M.; Korevaar, P. A. Self-Organization Emerging from Marangoni and Elastocapillary Effects Directed by Amphiphile Filament Connections. *Langmuir* **2022**, *38* (35), 10799–10809. https://doi.org/10.1021/acs.langmuir.2c01241.

https://doi.org/10.26434/chemrxiv-2024-qhmqn **ORCID:** https://orcid.org/0000-0002-3395-7197 Content not peer-reviewed by ChemRxiv. **License:** CC BY-NC-ND 4.0

(51) van der Weijden, A.; Winkens, M.; Schoenmakers, S. M. C.; Huck, W. T. S.; Korevaar, P. A. Autonomous Mesoscale Positioning Emerging from Myelin Filament Self-Organization and Marangoni Flows. *Nat Commun* **2020**, *11* (1). https://doi.org/10.1038/s41467-020-18555-w.

(52) Smith, T. G.; Lange, G. D.; Marks, W. B. Fractal Methods and Results in Cellular Morphology — Dimensions, Lacunarity and Multifractals. *J Neurosci Methods* **1996**, *69* (2), 123–136. https://doi.org/10.1016/S0165-0270(96)00080-5.

(53) Vella, D.; Mahadevan, L. The "Cheerios Effect." *Am J Phys* **2005**, *73* (9), 817–825. https://doi.org/10.1119/1.1898523.

(54) Bentov, S.; Brownlee, C.; Erez, J. The Role of Seawater Endocytosis in the Biomineralization Process in Calcareous Foraminifera. *Proceedings of the National Academy of Sciences* **2009**, *106* (51), 21500–21504. https://doi.org/10.1073/pnas.0906636106.

https://doi.org/10.26434/chemrxiv-2024-qhmqn **ORCID:** https://orcid.org/0000-0002-3395-7197 Content not peer-reviewed by ChemRxiv. **License:** CC BY-NC-ND 4.0